Applied Materials Today 32 (2023) 101832

Contents lists available at ScienceDirect

Applied Materials Today

journal homepage: www.elsevier.com/locate/apmt

Investigating the thickness-effect of free-standing high aspect-ratio TiO_2 nanotube layers on microwave-photoresponse using planar microwave resonators

Mahnaz Alijani [a,b], Benjamin D. Wiltshire [b], Hanna Sopha [a,c], Zahra Sarpanah [b], Jan Mistrik [c], Ludek Hromadko [a,c], Mohammad H. Zarifi [b], Jan M. Macak [a,c,*]

[a] Central European Institute of Technology, Brno University of Technology, Purkynova 123, Brno 61200, Czech Republic
[b] Okanagan MicroElectronics and Gigahertz Applications (OMEGA) Laboratory, School of Engineering, University of British Columbia, British Columbia V1V 1V7, Canada
[c] Center of Materials and Nanotechnologies, Faculty of Chemical Technology, University of Pardubice, Nam. Cs. Legii 565, Pardubice 53002, Czech Republic

ARTICLE INFO

Keywords:
Planar microwave resonator
TiO_2
Nanotube
Real-time microwave sensing
UV detection

ABSTRACT

One-dimensional TiO_2 nanotube (TNT) layers are a promising candidate for UV detection due to their distinctive anisotropic geometry which is effective for light harvesting and rapid carrier transport. Here, the photosensitivity efficiency of TNT layers with various thicknesses of 15, 50, 80, and 110 μm was utilized at a microwave frequency regime by modeling and experimentally. A planar microwave split ring resonator (PMSRR) was designed and fabricated to operate at ~8 GHz to study TNT layers by monitoring the scattering parameter (S_{21}) of the PMSRR under a constant UV irradiation power of ~96.4 μW/cm^2. According to the results, the 80 μm thick TNT layers demonstrated the highest resonant amplitude variation for the customized PMSRR. The change of the resonant amplitude was mainly attributed to the conductivity variation contributed by perturbation of trapped electron concentration, as the dominant factor under UV illumination, and their electromagnetic wave interaction. The main advantage of the proposed method of PMSRR for microwave photosensitivity monitoring over the conventional direct current (DC) conductivity measurements is to eliminate the effect of contact resistance between the TNT layers and metal electrodes utilizing the contactless aspect of wave interactions with the TNT layers at microwave regime to perform electrode-less measurements.

1. Introduction

Ultraviolet (UV) detectors have attracted considerable attention in numerous applications such as optoelectronic integrated circuits, optical communications, radiation detection, astronomical studies, memory storage, chemical and biological analysis, and food safety [1–6]. Excessive exposure to UV irradiation is deleterious and causes adverse health effects, for instance, premature skin damage and skin cancer [7]. Therefore, a highly sensitive device for the detection of UV irradiation is in great demand in a wide range of applications.

Recently, planar microwave resonator sensors have demonstrated attractive and robust performance providing high sensitivity, high signal-to-noise ratio (quality factor), real-time response, and simple operation for sensing and monitoring the presence of liquids, solids, or other large variations in the dielectric properties in their nearby environment [8,9]. These resonators can be integrated compactly using a low-cost fabrication process relative to cavity waveguide resonators; however, they require chemically or optically active materials to sensitize them to stimuli such as gasses or radiation [10]. Fortunately, the planar microwave resonators can easily be integrated with nanostructured materials to make them sensitive to UV irradiation via absorption and subsequent charge generation [9,11]. In recent years, nanostructured semiconductors such as nanorods, nanowires, and nanotubes have attracted extensive research interest due to their high surface-to-volume ratio and their designable and adjustable surface morphology [12–14] that can be applied to various surfaces or surface-to-volume sensitive applications. Sensor devices, integrated with nanostructured semiconductors, are usually characterized by photoconductivity measurements. They exhibit surface-dependent behavior and a long recovery time due to the presence of a carrier

* Corresponding author.
E-mail address: jan.macak@upce.cz (J.M. Macak).

https://doi.org/10.1016/j.apmt.2023.101832
Received 8 February 2023; Received in revised form 3 April 2023; Accepted 22 April 2023
Available online 27 April 2023

depletion layer at the nanomaterial surface caused by surface trap states [11,15]. Among various wide bandgap semiconductive metal–oxides, such as TiO_2, ZnO, SnO_2, and their nanostructures, one-dimensional TiO_2 nanotubes (TNTs) are favourable as highly efficient UV photodetectors, as they possess intrinsic UV-sensitive properties and high active surface area. Moreover, their unique hollow geometry enables increased charge trapping and a direct pathway for the rapid transport of photogenerated carriers [16–19]. Based on these factors, TNT layers constitute a promising platform for microwave permittivity measurements [10]. In earlier studies on microwave resonator sensors, the potential of high-resolution planar microwave resonator sensors integrated with TNT layers was investigated [8,10,11]. The mechanism of these sensors is based on the permittivity and conductivity variation in the TNT layers due to UV irradiation. By changing these dielectric properties of the integrated TNT layers, a shift in the sensor's resonant amplitude or resonant frequency can be observed [8]. In a pioneering work, Zarifi *et al.* [10] demonstrated that the changes in these parameters are dependent on both the incident light's wavelength and intensity. In a subsequent investigation, the dielectric properties of TNTs were studied to make material analysis convenient in both the illuminated and non-illuminated states [11].

The anodic TNT layers have tuneable tube diameter and layer thickness to provide to the demands of a wide range of applications [20]. A suitable parameter that characterizes the dimensionality of TNT layers is the aspect ratio, which is the ratio between TNT layer thickness and the average nanotube diameter. Until now, all reports regarding microwave resonator sensors used relatively low aspect ratio TNT layers [8,10,11]. However, recently a tailored protocol enabling the preparation of ultra-high aspect ratio (HAR) TNT layers in a very short time was reported [21,22]. This opens the door for their utilization as high-performance resonators with potentially superior sensing performance in the UV region. In particular, the TNT layer thickness is thought to affect the response due to its increased surface area, optical properties, and amenability towards functionalization. Overall, the high surface area heterojunction of the functionalized HAR TNTs can be the best candidate for this purpose with very attractive properties such as high sensitivity and selectivity. A thorough analysis of the sensing platform, the TNT layers and their effect on the sensing response is required, to obtain these benefits.

Therefore, in the present work, the effect of TNT layers thickness and aspect ratio on the sensor response is exploited to further understand and improve the performance of TiO_2-integrated microwave resonators for UV detection. The main purpose of this fundamental, but previously unexplored study, is to seek optimal TNT layers thickness, exploiting previously unattainable layers dimensions, and provide insight into the interaction between charge generation and microwave sensing upon UV irradiation.

2. Experimental section

The synthesis and characterization of TNT layers is presented in the Supplementary Information. Resonator design and operation: To monitor the dielectric properties variation (relative permittivity (ε_r) and conductivity (σ_r) in the TNT layers, a planar split-ring resonator (SRRs) was designed with a small gap in the ring structure to host the delaminated TNT layers, as shown in Fig. 1a. A single-ring design was chosen to simplify the analysis and enable the development of an analytical model for further understanding and exploiting the influence of the thickness of TNT layers on the resonator's response. The transmission power (S_{21}) was measured as the main electrical parameter, which was the ratio of

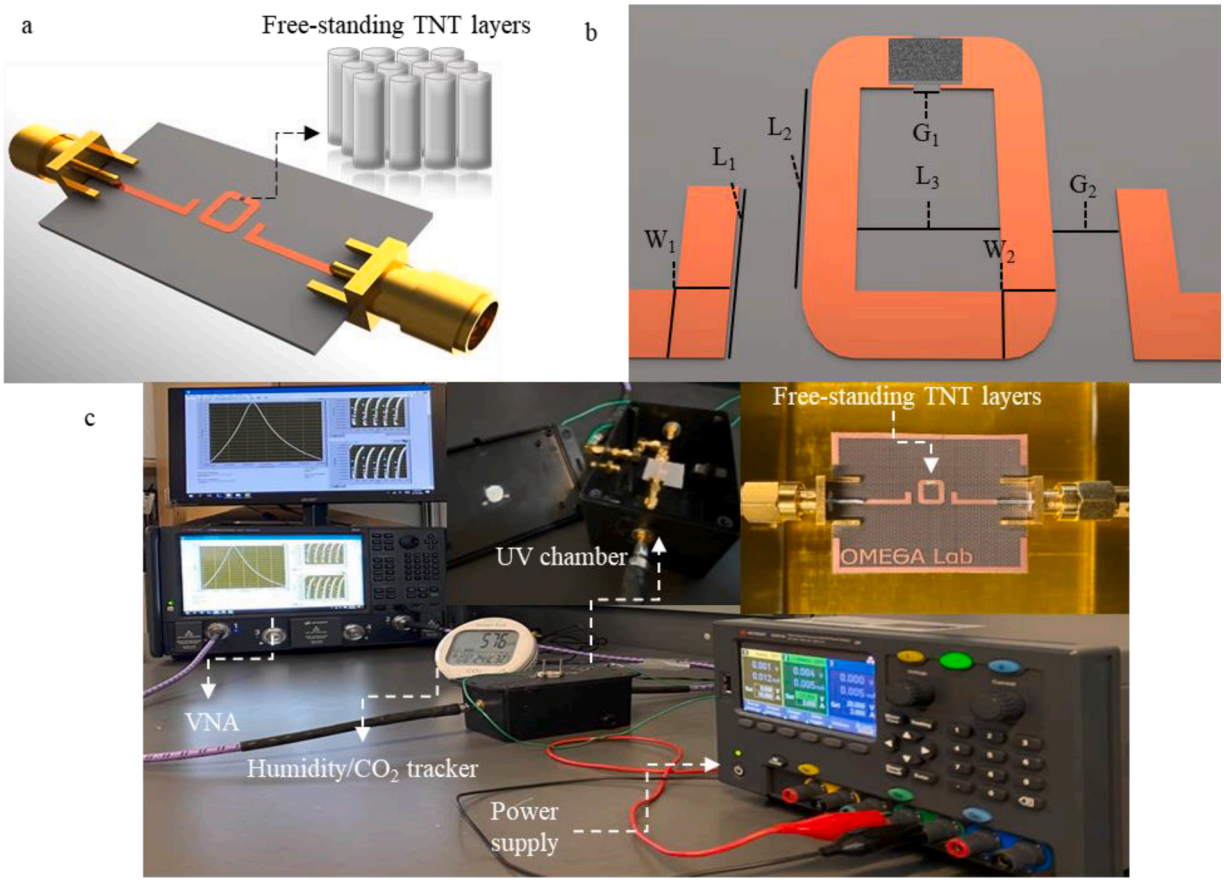

Fig. 1. (a) The resonator design with the TNT layers placement in the ring gap; (b) dimensions of the resonator sensor in mm: $W_1 = W_2 = 0.9$, $L_1 = 2.4$, $L_2 = 3.1$, $L_3 = 2.5$, $G_1 = 0.25$, $G_2 = 1.2$; (c) Instrumentation and experimental setup with the fabricated microwave resonator shown in the inset.

the transmitted power through the resonator with the delaminated TNT layers to the incident microwave power, and the resonant amplitude and frequency were extracted from the S_{21} measurements. The resonator was designed to operate in X-band to align with the small size of the TNT layers [23–25], where the dimensions of the resonator were estimated using Eq. (1), which equates the resonant frequency to the dimensions and the material properties of the resonator and its nearby environment [26].

$$f_0 = \frac{c}{2L\sqrt{\varepsilon_{eff}}} \quad (1)$$

Where f_0 is the resonant frequency of the structure, c is the vacuum speed of electromagnetic radiation ($\sim 3 \cdot 10^8$ m/s), L is the path length of the resonant ring structure, and ε_{eff} is the effective permittivity in near environment of the resonator, usually approximated by the substrate permittivity.

The resonator with estimated size was then implemented and simulated in *Ansys HFSS* software to have a resonant frequency and a resonant amplitude of ~8.45 GHz and ~−20 dB, respectively, shown in Fig. 1b. The frequency was chosen to allow for a compact design without requiring lithographic or complex fabrication processes, while also avoiding loss or noise due to water or humidity signal attenuation, which are more pronounced at lower frequencies [27,28]. The designed and simulated resonator was fabricated using a chemical etching process on a Rogers 5880 substrate with permittivity of 2.20 and loss tangent of 0.0009, with a copper cladding thickness of 35 μm.

A Vector Network Analyzer (VNA, Keysight N5222B) calibrated with a Keysight e-cal kit (N4691D) was used to measure the microwave signals. For the experimental purposes, the output power of the VNA was set to 0 dBm (~1 mW), so as not to heat the sample, with 300 Hz IFBW to measure 4001 equally spaced data points between 8.1 and 8.9 GHz. The resonator was placed within a semi-sealed and opaque chamber to prevent external light from interfering with the TNT layers during the experiments, and to avoid humidity and temperature variation. A voltage controlled adjustable intensity UV LED was placed at a constant distance of 5 cm above the resonator to illuminate the TNT layers. The LED was controlled via a power supply (Keysight E36200) under a constant DC current of 20 mA (providing 96.4 μW/cm^2). LabVIEW software was used to record the S_{21} response at 15 s intervals for the duration of the experiment. The experimental setup is presented in Fig. 1c with the resonator chamber and the TNT alignment shown as an inset.

3. Results and discussion

Fig. 2 presents SEM cross-sectional and top view (inset) images of TNT layers with different thicknesses grown on Ti foils. In particular, these images were taken to illustrate the dimensions of the nanotubes including thickness, diameter, and aspect ratio resulting from the different electrochemical anodization processes listed in Table 1. As can be seen, the TNT layers are composed of well-aligned nanotubes that are very well cross-connected.

XRD characterizations were carried out to analyze the crystalline structure of TNT layers after the annealing process. XRD results for each different TNT thickness are presented in Fig. 3 with the associated peaks of anatase (A) and metallic titanium (Ti) included according to PDF database (PDF 04–011–0664 for anatase and PDF 00–071–0859 for Titanium). The Miller indices (hkl) are also displayed in Fig. 3 for all the obtained peaks. The Ti peaks clearly seen in the pattern of 15 μm thick TNT layers stem from the underlying Ti substrate, which is used to hold all substrates during XRD measurements, and is still visible to X-rays. However, with the increasing thickness of layers, these signals fade out and only anatase signal remains present in the patterns.

The anatase crystallite sizes (d) were estimated from XRD patterns using Scherrer line-broadening approach and are presented in Table 1.

Prior to analyze the microwave photoconductivity performance of the TNT layers, a baseline measurement of S_{21} was performed with and without TNT layers, and the rest of the microwave results were

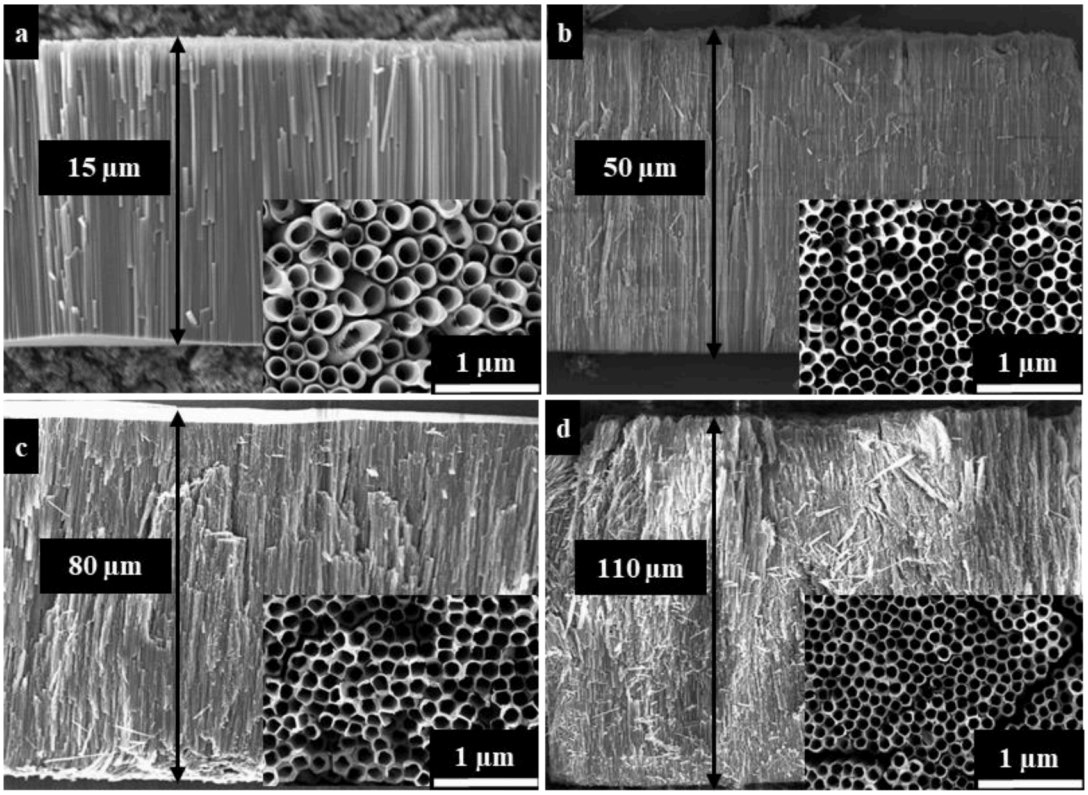

Fig. 2. SEM cross-sectional and top views (inset) images of the TNT layers of different thicknesses (a) 15 μm, (b) 50 μm, (c) 80 μm, (d) 110 μm.

Table 1
Average thicknesses, inner diameters, and aspect ratios of the TNT layers with the corresponding anodization conditions: electrolyte, potential, and anodization time.

Average thickness (μm)	Average diameter (nm)	Average aspect ratio	Electrolyte composition	Anodization potential (V)	Anodization time (min)	Crystallite size (Å)
15	250	60	EG, 10% H_2O and 0.15 M NH_4F [29]	100	240	245
50	195	256	1 M LA, 0.176 M NH_4F and 1.5 vol%		30	234
80	200	400	H_2O [21]		90	269
110	150	733			120	302

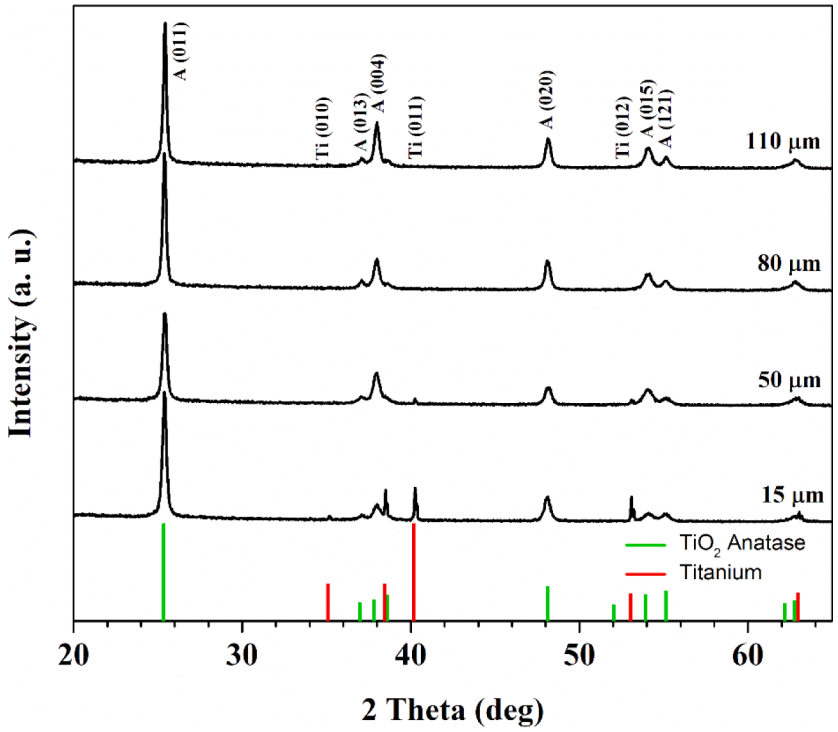

Fig. 3. XRD patterns of TNT layers with different thicknesses (15, 50, 80, 110 μm) annealed at 400 °C for 1 h in air. PDF-4+ ICDD codes are 154,603 for TiO_2 anatase and 653,280 for Titanium.

compared to these based lines while the TNT layer is on the planar microwave split ring resonator and in a dark environment. The scattering parameter (S_{21}) results are shown in Fig. 4 and was compared to FEM simulated structure in HFSS software. A 50 μm thick TNT layer was chosen to illustrate S_{21} variation in response to material inclusion at the ring gap.

Fig. 4 shows a closely matched resonant frequency and amplitude in the simulated and adding an arbitrary TNT layers of a 50 μm thickness on the ring gap of the resonator affected the resonant profile (S_{21}) due to the effective permittivity of the TNT layers (~10) [10,30].

To investigate the photoconductivity efficiency of the HAR TNT layers, individual layers were placed sequentially over the ring gap of the resonator (as shown in Fig. 1a). Initially, 3 min baseline measurement of the resonator's response was recorded for normalization and TNT-resonator system characterization in absence of UV light. Then, the experiments were followed by 5 min illumination of the UV LED (390 nm, 96.4 μW/cm^2). Based on the bandgap of anatase TiO_2 (~3.2 eV) and the UV LED photon energy (3.4 eV), the microwave complex conductivity of TNT layers was increased over time due to increase in the concentration of changed carriers within the HAR TNT layers. After the UV irradiation period and during the recovery period, the resonant profile of the microwave SRR device returned to the baseline due to charge recombination within 20 min of halting the UV illumination. The process was repeated 4 times for each TNT layers with different thicknesses to ensure the reproducibility and consistency of the measured results. To compare the microwave photoconductivity of different HAR TNT layers, this process was performed with different TNT thicknesses of 15, 50, 80, and 110 μm. Results were collected in 15 s intervals using LabVIEW software and the resonant amplitude, resonant frequency, and quality factor were extracted from the resonant profile of the SRR. Performing the curve-fitting on the extracted resonant frequency and resonant amplitude versus time, time constants during the illumination (excitation period) and after the illumination (recovery period) were extracted to provide an insight on charge kinetics within the TNT layers including recombination rates, defect concentration, or trap lifetimes [31,32]. An illustrative summary of the changes in the resonant properties (resonant amplitude, resonant frequency) is shown in Fig. 5. Figures S1-S4 show all detailed time-variable results, namely time constants (excitation time constant: τ_{exc} and recombination time constant: τ_{Ret}), as well as average resonant amplitude shift (ΔA) and resonant frequency shift (Δf) for each thickness of the TNT layers.

The UV-stimulated microwave photoconductivity variation was reflected on microwave resonator's responses and was presented in Fig. 5 (and in Figs S1-S4) and was in accordance with S_{21} trends previously presented using TiO_2-based microwave studies [10,33]. In Fig. 5a, the non-illuminated 80 μm TNT layers resonant responses (normalized to 0 resonant amplitude and resonant frequency change) were compared with their responses after the full 5 min interval of UV irradiation, where the resonator demonstrated the maximum variation from the baseline, the dark response. The illumination of TNT layers above the resonant ring resulted in a decrease in resonant amplitude and frequency as the conductive and polarizable charge carriers were excited in the TNT

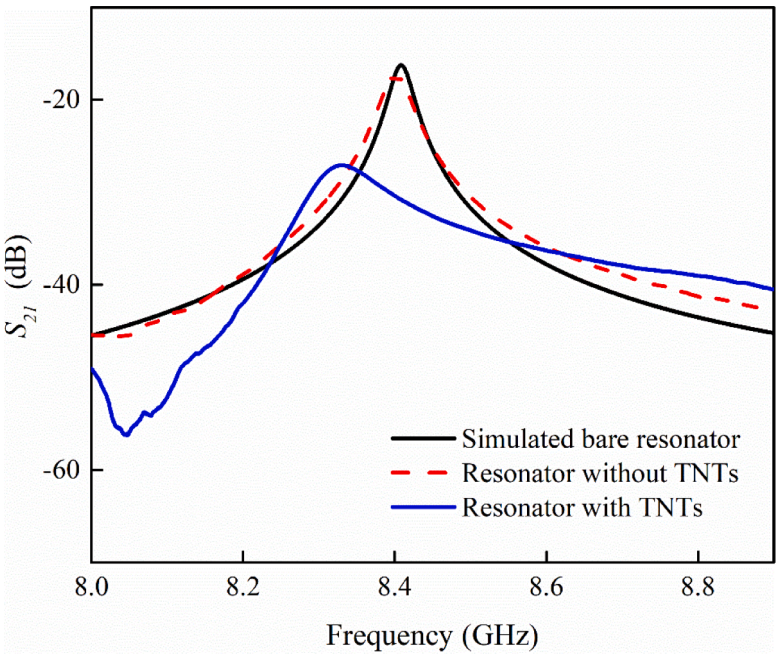

Fig. 4. Simulation results of the bare resonator (black, solid) compared with the fabricated resonator with TNT layers (red, dashed) and without TNT layers (blue, solid).

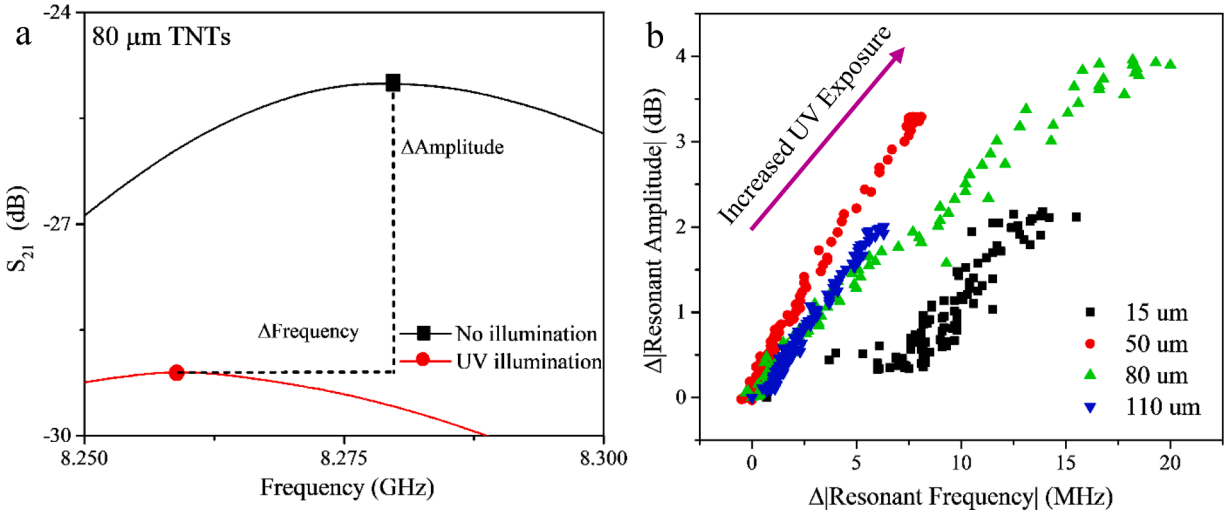

Fig. 5. (a) The changing S_{21} magnitude and frequency of the 80 μm TNT layers without illumination (normalized to 0) and after 5 min UV irradiation and (b) the transient change in resonant amplitude and frequency of each TNT layers under a UV irradiation cycle.

layers [34].

Fig. 5b presents the change in the resonant properties as the TNT was illuminated with UV light for 5 min and then allowed to return to baseline for 20 min. From Fig. 5b, it is apparent that the largest shift in S_{21} responses (both resonant amplitude and frequency) was achieved for the 80 μm thick TNT layers, and that was consistent over multiple measurements as demonstrated in Figs S1-S4.

Fig. 6 presents the microwave responses of the UV-exposed TNT layers with different thicknesses. According to the measured results of Fig. 6, increasing the thickness of the TNT layers from 15 μm to 80 μm increased the resonant amplitude (Fig. 6a) and the resonant frequency of the SRR's response (Fig. 6b). However, further increasing the thickness of the layers beyond 80 μm had an adverse impact on the change of the microwave parameters. Using the curve fitting method, the excitation time constants and recovery time constants were extracted for different layers on the different repeat of the experiments and were presented in Fig. 6c,d. According to these plots, no significant change was observed between the time constants of the layers with different thicknesses, which could be attributed to the thickness independence of the effective UV irradiation penetration to the layers (Fig. 6c) and surface and trapped electron concentrations in TNT layers (Fig. 6d).

To gain more insight into the properties of TNT layers, photocurrent measurements, Mott-Schottky, and diffuse reflectance measurements were carried out on TNT layers attached to the underlying Ti substrate (due to the electrical contact and mechanical support). Fig. S5 shows results of photocurrent measurements, which clearly indicate a decrease in generated photocurrent densities with increasing TNT layer thickness. This trend can be explained by the increasing number of traps and defects in thicker TNT layers (due to the longer travel distance of electrons) and the increased chance of trapping of the electrons in the TiO_2 walls [35–37]. Fig. 6c,d confirms that the thicker TNT layers require longer time constants for the UV penetration and the charge-recombination

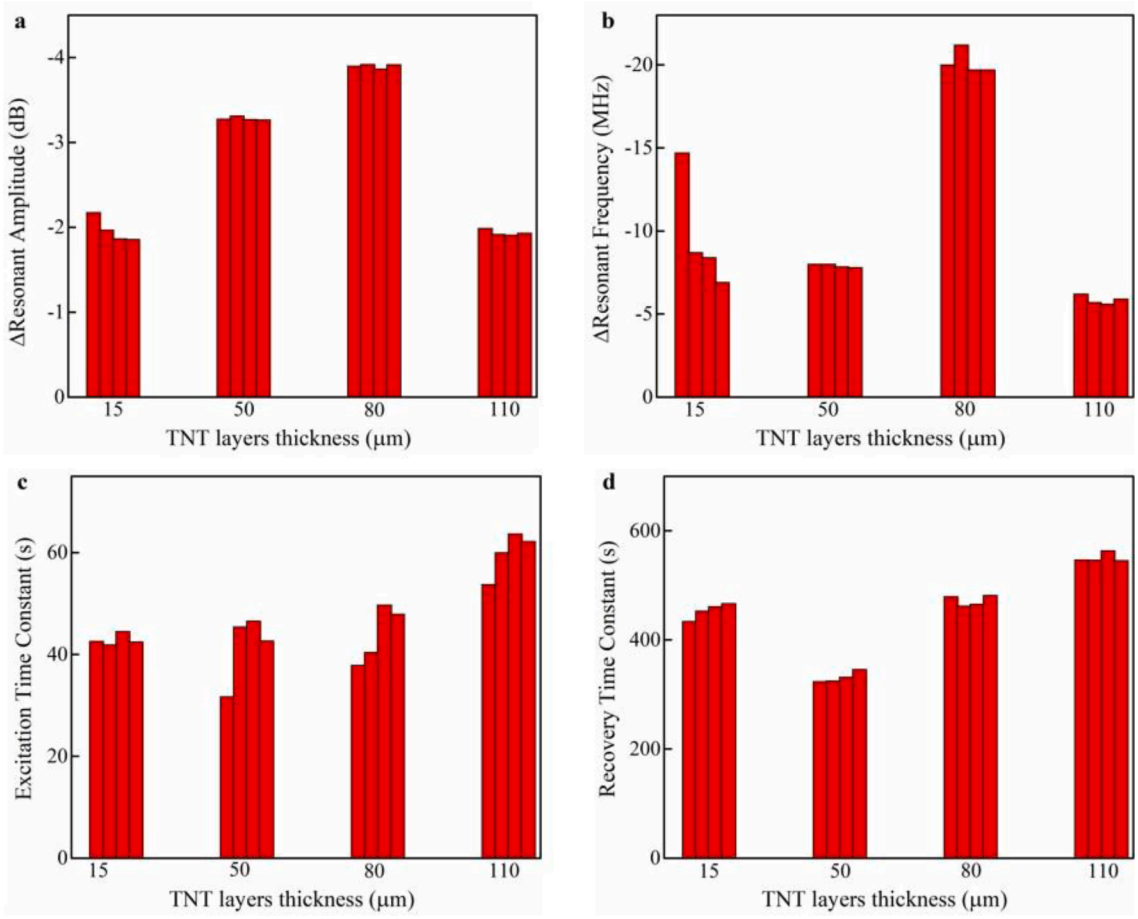

Fig. 6. Collected experimental results for 4 repeated measurements of free-standing layers of TNT with different thicknesses (15, 50, 80, 110 μm) for the resonant amplitude shift (a), resonant frequency shift (b), excitation time constant(c), and recovery time constant (d) upon UV irradiation for 5 min.

process, respectively, in comparison to their thinner counterparts, whereas Fig. 6.a, b present the amount of the light-stimulated charge carriers and their interactions with the electromagnetic waves for different TNT layers.

Fig. S6 shows diffuse reflectance measurements across the UV and VIS spectral regions and calculation of the optical band gap. The shape of recorded curves for the TNT layers confirmed the accuracy of the analysis compared to the previously reported spectra in the literature [38,39]. Based on the Kubelka-Munk function, all TNT layers demonstrated analogous optical band gaps of ~3.1 eV. Finally, Mott-Schottky measurements, as shown in Table S1, revealed that flat band potentials (E_{FB}) and majority charge carrier density (N_D) had also very clear trends with increasing thickness of TNT layers.

Furthermore, the recovery time constant (shown in Fig. 6d), which is mainly based on trap lifetimes and defect densities[35,40], could be related to the crystallite size as a larger crystallite size corresponded to a longer recombination time (see Table 1). This could be caused by a decrease in trap-assisted recombination in TNT layers with larger crystallite sizes and may indicate that intentionally decreasing crystallite size through processing may increase the speed of sensor operation [41].

3.1. Analytical modeling and FEM simulations

To understand the microwave photoresponse performance of the HAR TNT layers with different thicknesses, building a microwave resonator with a simple structure and analyzing E-field distribution is paramount. Therefore, the resonator model is implemented in HFSS software to perform finite element method analyses and to match the simulation results with the measured results (Fig. 7a). The E-field on an XY plane, 35 μm above the substrate and tangential to metal microstrip lines, is analyzed to find the region with the maximum E-field density, which also has the maximum sensitivity to TNT layers' dielectric properties variations. (Fig. 7b). The magnitude of the E-field on the dash line (shown in Fig. 8d), is plotted which confirms the maximum E-field at the gap of the SRR structure.

To study the impact of the thickness of the TNT layers and the electromagnetic field's interaction with UV photoresponse, E-field on the Z-axis, along the side of TNTs and perpendicular to the surface of the resonator is analyzed and extracted for the resonator with and without TNT layers (Fig. 7c). The curve fitting is applied, and the E-field distribution demonstrates a good matching with $Ez= a/(z^2+b^2)^{1/2}$ for the $a =$ 2 V, $b = 0.25$ mm for air (without TNT layers). The curve fitting results are aligned with the assumptions that will be made in theoretical analysis to support Eq. (5).

Exposing the TNT layers to UV light could be formulated based on light absorption, which generates excited charge carriers with contribution from perturbation of free electrons concentration, the excited electrons from the valence band to the conduction band, and from the perturbation of trapped electron concentration [34]. The UV penetration to the TNT layers could be modeled employing the Beer-Lambert Law, which is used for the light absorption in linear optics, to demonstrate the light intensity reduction in the TNT layers from their top surfaces Eq. (2):

$$I = I_0 e^{-\alpha z} \tag{2}$$

Where I is the intensity of light as it varies within a material due to absorption, I_0 is the incident intensity after the reflection losses are

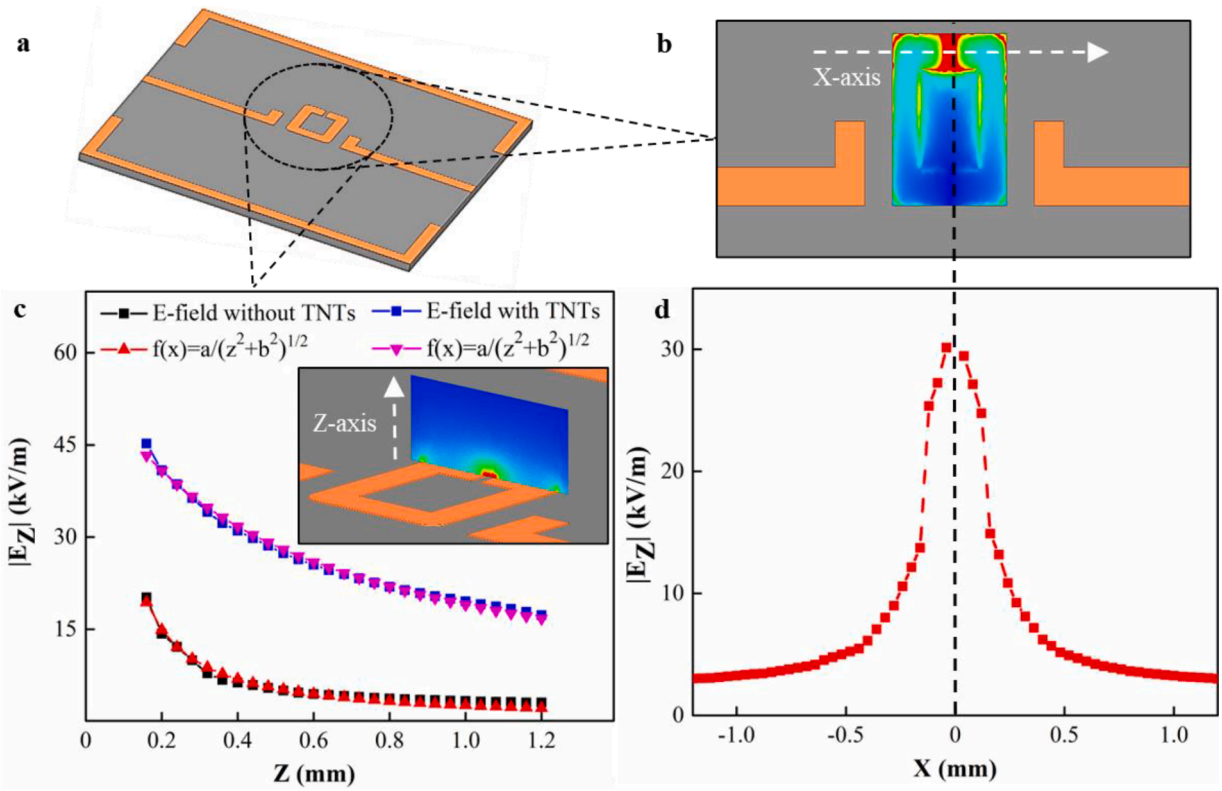

Fig. 7. (a) implemented structure in HFSS, similar to the fabricated sensor, (b) electric field analysis in X-axis tangential to the surface of the sensor, c) electric field analysis perpendicular to the resonator's surface, comparing E-field distribution for a resonator without (ε_r =1) and with TNT layers (ε_r =10, with no loss), (d) E-field analysis perpendicular to the surface of resonator along X-axis.

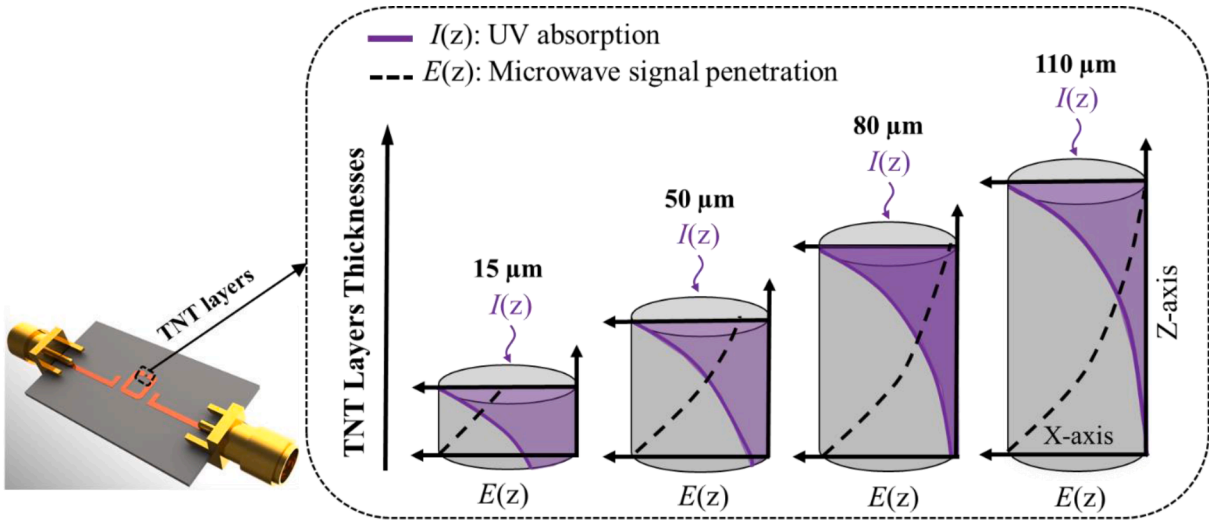

Fig. 8. Generated patterns of UV adsorption (purple) and microwave signal penetration (dashed) showing their region of interaction for various TNT thicknesses (15, 50, 80, 110 µm).

considered, z is the depth within the material, and α is the frequency-dependent absorption coefficient of the material. The light penetration depth within the nanotubular TiO_2 is approximately ~20 µm, where the intensity reached 50% of I_0 (considering the absorption coefficient of TiO_2 nanotubes is 0.04 μm^{-1} at the incident wavelength of 390 nm) [36]. This means that for the 15–110 µm thick TNT layers used in this work, there is a large variation in the UV absorption and consequently a significant difference on photoconductivity variation across the layers [36]. To understand Eq. (2) in terms of excited charge carriers, we can calculate the changing optical intensity and attribute that to charge carrier generation, G, as shown in Eq. (3) [42].

$$G = \frac{d}{dz}(I) = -\alpha I_0 e^{-\alpha z} \tag{3}$$

It is worth mentioning that in this work, the vertically aligned TNT layers were illuminated by the UV light from their top part, where the microwave signal was penetrating from the bottom of the layers. This situation was schemed and simulated in Fig. 8. The microwave signal interacted with the TNT layers from the bottom, this interaction from opposing sides is later illustrated and discussed due to its importance on

charge-microwave interaction.

Previous studies [10,43,44], have confirmed that the increase in the charge carrier concentration affects both the resonant frequency and the resonant amplitude of a microwave resonator. Illuminating the UV light changes the complex permittivity of the TNT layers according to Eq. (4):

$$\varepsilon_r = \varepsilon_r^{'} - i\varepsilon_r^{''} = \varepsilon_r^{'} - i\frac{\sigma}{\varepsilon_0 \omega} \tag{4}$$

As observed in the measured responses of the microwave device, both the resonant frequency and the resonant amplitude are changed, which could be related to changes in the real and imaginary components of the complex permittivity, respectively. It has been proven that the perturbation of both free and trapped electrons could contribute to the complex permittivity variation, where in microwave regime perturbation of the trapped electrons is dominant and can increase the number of polarizable charges that consequently reduces the resonant frequency [34].

This could increase the effective permittivity of the layers and reduce the resonant frequency based on Eq. (1) Similarly, the increase in trapped charges increased the overall conductivity of the material, leading to a decrease in the resonant amplitude (increased signal loss), as conductive charges were able to convert some of the microwave energy into motion or vibration [45].

To study the effect of TNT thickness, and due to the comparatively low frequency, the microwave signal follows the static field approximation of a dipole positioned along the gap region (surface charge distribution along the cross-section of microstrip-line) as shown in Eq. (5), which also uses results from the HFSS simulations (Fig. 7c).

$$|\mathbf{E}| \propto \frac{q}{\varepsilon\left(z^{'2} + \frac{g^2}{4}\right)^{0.5}} \tag{5}$$

Where $|\mathbf{E}|$ is the microwave signal strength in a material with the effective permittivity of ε originated by a dipole of opposite charges of q (to keep the model simple, the effect of loss factor "tanD" was disregarded). Due to layers placement in the center of the gap, the field strength is measured at the halfway point between the gap, $g/2$, and at a depth $z^{'}$ where $z^{'}$ is measured from the bottom of the layers. Combining Eqs. (3) and (5) can quantify the microwave-charge coupling interaction at a TNT depth, z, as follows in Eq. (6).

$$\phi = G\,|\mathbf{E}| = \frac{-\alpha q I_0 e^{-\alpha z}}{\varepsilon\left(z^{'2} + \frac{g^2}{4}\right)^{0.5}} \tag{6}$$

Where we define ϕ as the magnitude of charge coupling between generated carriers, G, in a region along the TNT layers with the microwave field strength $|\mathbf{E}|$. Graphically this is visualized with limiting cases in Fig. 8 with the important note that z and z' position parameters were measured from opposing ends of the TNTs ($z^{'}$ = L - z).

Based on previous works it is apparent that very thick substrate or membrane layers will exhibit weaker interaction because light absorption and field penetration do not exist strongly in the same region. Eqs. (3) and (5) indicate that both microwave and UV radiation intensities decrease monotonically as the signal moves further along the TNT axis, leading to charge/microwave separation, where both signals decrease to small values at the large z limit. In the extreme case, for very long TNTs, the UV would be completely absorbed at the top surface of the TNT, while the microwave signal was interacting with only the bottom of the TNT with the net result being that generated charges do not interact with the sensing microwave signal because they exist in different regions of the TNTs.

In contrast, thinner TNT layers would have high charge generation efficiency, but due to their smaller volume the majority of the UV signal will pass through without being absorbed ($I \approx I_0$) and very few electron-hole pairs will be generated to interact with the input microwave signal, leading to non-optimal (low) sensitivity [10]. To quantify the charge-microwave coupling versus the thickness of the TNT layers, we integrate ϕ from (6) over the entire layers thickness (called microwave light interaction score Θ), where the score effectively includes all generated charges and their interaction with the microwave signal. Microwave light interaction score is represented mathematically in Eq. (7) and implemented in a MATLAB code (included in SI) to compare the scores between TNTs with different thicknesses and to the experimental results in Fig. 9a,b.

$$\Theta = \int_0^L \phi dz^{'} = \int_0^L \frac{-\alpha q I_0 e^{-\alpha(L-z^{'})}}{\varepsilon\left(z^{'2} + \frac{g^2}{4}\right)^{0.5}} dz^{'} \tag{7}$$

According to the experimental and FEM modeling results of Fig. 9, it is shown that for low and high thicknesses of TNT layers, the microwave light interaction score decreases. Instead, there is an optimal TNT layers thickness range, where sensitivity to UV light is at maximum. Using values from recent literature to represent Eq. (7) graphically, the optimum TNT layers thickness was calculated to be 77 μm, which is a good match with the responses of the measured microwave parameters.

4. Conclusion

This work studied microwave photoconductivity efficiency of length variant TNT layers (15, 50, 80, and 110 μm) at X- band (~8 GHz) for possible sensing and wireless space communication applications. Anatase TNT layers were integrated with a planar SRR microwave resonator that was designed, simulated, and fabricated to evaluate the microwave photoconductivity performance of the TNT layers. Transient time experiments were performed to record the resonant amplitude, frequency, and quality factor variation of the resonator over time as the TNT layers were illuminated with a constant UV light. Microwave signal parameters such as the resonant amplitude demonstrated a maximum sensitivity of 0.04 dB/μWcm^{-2} over 4 measurement cycles for all HAR TNT layers. Additionally, transient parameters of the microwave signals, such as time constants, settling times, and lag times, were extracted using the curve fitting method to correlate the time-based microwave photoconductivity activities of the TNT layers to their thicknesses. These findings were aligned with the XRD measurements, which confirmed a correlation between the crystallite sizes and the photoconductivity efficiency of the TNT layers.

In conclusion, the microwave photoconductivity behavior of the TNT layers with various thicknesses demonstrated the most significant change at 80 μm thick TNT layers both in the resonant amplitude and the resonant frequency responses on the custom-made microwave resonator compared to the other layers' thicknesses. These experimental results were closely aligned with the constructed theoretical model, where the effects of light absorption and microwave field penetration depth indicated the optimal TNT length of 77 μm, approximately. Furthermore, it was shown that the shorter or longer TNTs than the optimized length of the TNT layers (80 μm) would suffer from insufficient light absorption or weak photoconductivity-electromagnetic wave interaction.

Supporting information

Supporting information is include experimental section, microwave measurements, modeling code, and supporting analysis (Photocurrent measurements) (Microsoft Word file).

Author contributions

All authors have given approval for the final version of the manuscript.

Data statement

Data used to create this work can be shared based on a reasonable request.

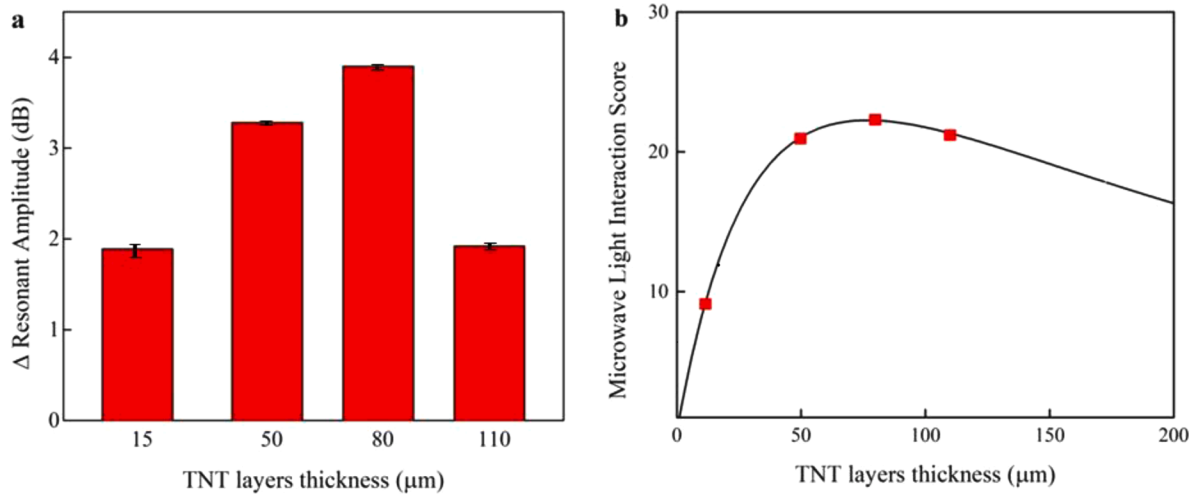

Fig. 9. Resonant amplitude shift of different TNT layers thicknesses (15,50,80,110 μm): (a) as measured and (b) modelled using α from literature (0.04 μm^{-1}) and g from the designed structure (0.25 mm), error bars represent the standard deviation of the resonant amplitude shift measured over the 4 sweeps, as recorded in SI.

CRediT authorship contribution statement

Mahnaz Alijani: Conceptualization, Investigation, Visualization, Writing – original draft, Writing – review & editing. **Benjamin D. Wiltshire:** Investigation, Visualization, Writing – original draft. **Hanna Sopha:** Investigation, Visualization, Writing – review & editing. **Zahra Sarpanah:** Investigation, Visualization. **Jan Mistrik:** Investigation, Visualization. **Ludek Hromadko:** Investigation, Visualization, Writing – review & editing. **Mohammad H. Zarifi:** Conceptualization, Supervision, Funding acquisition, Project administration, Writing – review & editing. **Jan M. Macak:** Conceptualization, Supervision, Funding acquisition, Project administration, Writing – review & editing.

Declaration of Competing Interest

The authors declare that they have no known competing financial interests or personal relationships that could have appeared to influence the work reported in this paper.

Acknowledgment

The authors acknowledge the Ministry of Education, Youth and Sports of the Czech Republic (MEYS CR, LM2018103, CZ.02.1.01/0.0/0.0/17_048/0007421). M.A. would like to thank junior grant projects 2021−2022 (CEITEC VUT-J-21-7397) and 2022–2023 (CEITEC VUT-J-22-8078) of Brno University of Technology. B.D.W. would like to thank NSERC CGS D scholarship support (no.535553). The authors acknowledge the Syilx Okanagan Nation for use of their unceded territory, the land on which the research was conducted. The authors acknowledge support from the Natural Sciences and Engineering Research Council of Canada (NSERC) through grant RGPIN-2018-04288. The authors thank the Mathematics of Information Technology and Complex Systems (Mitacs) Accelerate program through grant nos. IT19272, IT12995, and IT16696. The authors thank Canadian Foundation for Innovation (CFI) through grants no. 38148 as well as CMC microelectronics for their software licenses. SEM analyses were carried out with the support of CzechNanoLab Research Infrastructure (LM2018110, MEYS CR, 2020–2022).

Supplementary materials

Supplementary material associated with this article can be found, in the online version, at doi:10.1016/j.apmt.2023.101832.

References

[1] T. Bintsis, E. Litopoulou-Tzanetaki, R.K. Robinson, Existing and potential applications of ultraviolet light in the food industry - a critical review, J. Sci. Food Agric. 80 (2000) 637–645, https://doi.org/10.1002/(SICI)1097-0010(20000501)80:6<637::AID-JSFA603>3.0.CO;2-1.
[2] S. Yang, J. Gong, Y. Deng, A sandwich-structured ultraviolet photodetector driven only by opposite heterojunctions, J. Mater. Chem. 22 (2012) 13899–13902, https://doi.org/10.1039/c2jm32287k.
[3] E. Monroy, F. Omnès, F. Calle, Wide-bandgap semiconductor ultraviolet photodetectors, Semicond. Sci. Technol. 18 (2003), https://doi.org/10.1088/0268-1242/18/4/201.
[4] Y. Zou, Y. Zhang, Y. Hu, H. Gu, Ultraviolet detectors based on wide bandgap, (2018) 1–25. doi:10.3390/s18072072.
[5] R.A. Alahnomi, Z. Zakaria, Z.M. Yussof, A.A. Althuwayb, A. Alhegazi, H. Alsariera, N.A. Rahman, Review of recent microwave planar resonator-based sensors: techniques of complex permittivity extraction, applications, open challenges and future research directions, Sensors (Basel) 21 (2021) 2267, https://doi.org/10.3390/s21072267.
[6] A. Salim, S. Lim, Review of recent metamaterial microfluidic sensors, Sensors 18 (2018) 232, https://doi.org/10.3390/s18010232.
[7] Y. Ke, X. Wang, TGF b signaling in photoaging and UV-induced skin cancer, J. Invest. Dermatol. 141 (2021) 1104–1110, https://doi.org/10.1016/j.jid.2020.11.007.
[8] B.D. Wiltshire, M.H. Zarifi, TiO2 nanotube-integrated microwave planar resonator sensor for ultraviolet transmission-based liquid characterization, Sens. Actuat. B Chem. 341 (2021), 130014, https://doi.org/10.1016/j.snb.2021.130014.
[9] B.D. Wiltshire, M. Alijani, S. Mohammadi, A. Hosseini, J.M. Macak, M.H. Zari, High-frequency TiO 2 nanotube-adapted microwave coplanar waveguide resonator for high-sensitivity ultraviolet detection, (2022). doi:10.1021/acsami.1c21741.
[10] M.H. Zarifi, A. Mohammadpour, S. Farsinezhad, B.D. Wiltshire, M. Nosrati, A. M. Askar, M. Daneshmand, K. Shankar, Time-resolved microwave photoconductivity (TRMC) using planar microwave resonators: application to the study of long-lived charge pairs in photoexcited titania nanotube arrays, J. Phys. Chem. C. (2015), 150615093503007, https://doi.org/10.1021/acs.jpcc.5b01066.
[11] M.H. Zarifi, B. Wiltshire, N. Mahdi, P. Kar, K. Shankar, M. Daneshmand, Ultraviolet sensing using a TiO 2 nanotube integrated high resolution planar microwave resonator device, Nanoscale 10 (2018) 4882–4889, https://doi.org/10.1039/C7NR06869G.
[12] Y. Xie, L. Wei, Q. Li, Y. Chen, S. Yan, J. Jiao, G. Liu, L. Mei, High-performance self-powered UV photodetectors based on TiO2 nano-branched arrays, Nanotechnology 25 (2014), https://doi.org/10.1088/0957-4484/25/7/075202.
[13] T. Zhai, X. Fang, M. Liao, X. Xu, H. Zeng, B. Yoshio, D. Golberg, A comprehensive review of one-dimensional metal-oxide nanostructure photodetectors, Sensors 9 (2009) 6504–6529, https://doi.org/10.3390/s90806504.
[14] Y.-F. Sun, S.-B. Liu, F.-L. Meng, J.-Y. Liu, Z. Jin, L.-T. Kong, J.-H. Liu, Metal oxide nanostructures and their gas sensing properties: a review, Sensors (Basel) 12 (2012) 2610–2631, https://doi.org/10.3390/s120302610.
[15] Z. Li, Z. Li, C. Zuo, X. Fang, Application of nanostructured TiO2 in UV photodetectors: a review, Adv. Mater. (2022), 2109083.
[16] S. Ng, P. Kuberský, M. Krbal, J. Prikryl, V. Gärtnerová, D. Moravcová, H. Sopha, R. Zazpe, F.K. Yam, A. Jäger, L. Hromádko, L. Beneš, A. Hamáček, J.M. Macak, ZnO coated anodic 1D TiO 2 nanotube layers: efficient photo-electrochemical and gas sensing heterojunction, Adv. Eng. Mater. 20 (2018), 1700589, https://doi.org/10.1002/adem.201700589.
[17] S. Ng, J. Prášek, R. Zazpe, Z. Pytlíček, Z. Spotz, J.R. Pereira, J. Michalička, J. Přikryl, M. Krbal, H. Sopha, J. Hubálek, J.M. Macák, Atomic layer deposition of

SnO2-coated anodic one-dimensional TiO2 nanotube layers for low concentration NO2 sensing, ACS Appl. Mater. Interfaces. 12 (2020) 33386–33396, https://doi.org/10.1021/acsami.0c07791.
[18] A. Mohammadpour, P. Kar, B.D. Wiltshire, A.M. Askar, K. Shankar, Electron transport, trapping and recombination in anodic TiO2 nanotube arrays, (n.d.). http://www.ingentaconnect.com/contentone/ben/cnano/2015/00000011/00000005/art00008 (accessed March 4, 2018).
[19] M.H. Zarifi, S. Farsinezhad, M. Abdolrazzaghi, M. Daneshmand, K. Shankar, Selective microwave sensors exploiting the interaction of analytes with trap states in TiO $_2$ nanotube arrays, Nanoscale 8 (2016) 7466–7473, https://doi.org/10.1039/C5NR06567D.
[20] S.P. Albu, A. Ghicov, J.M. Macak, R. Hahn, P. Schmuki, Self-organized, free-standing TiO2 nanotube membrane for flow-through photocatalytic applications, Nano Lett. 7 (2007) 1286–1289, https://doi.org/10.1021/nl070264k.
[21] M. Alijani, H. Sopha, S. Ng, J.M. Macak, High aspect ratio TiO2 nanotube layers obtained in a very short anodization time, Electrochim. Acta. (2021), 138080, https://doi.org/10.1016/j.electacta.2021.138080.
[22] M. Alijani, H. Sopha, S. Ng, J. Rodriguez-Pereira, J.M. Macak, High-aspect-ratio TiO 2 nanotube layers via galvanostatic anodization in an electrolyte containing lactic acid, Phys. Status Solidi – Rapid Res. Lett. 15 (2021), 2100146, https://doi.org/10.1002/pssr.202100146.
[23] W. Irshad, D. Peroulis, A 12–18GHz electrostatically tunable liquid metal RF MEMS resonator with quality factor of 1400–1840, in: 2011 IEEE MTT-S International Microwave Symposium, 2011, pp. 1–4, https://doi.org/10.1109/MWSYM.2011.5972971.
[24] S. Mohammadi, B. Wiltshire, M.C. Jain, A.V. Nadaraja, A. Clements, K. Golovin, D. J. Roberts, T. Johnson, I. Foulds, M.H. Zarifi, Gold coplanar waveguide resonator integrated with a microfluidic channel for aqueous dielectric detection, IEEE Sens. J. 20 (2020) 9825–9833, https://doi.org/10.1109/JSEN.2020.2991349.
[25] M.H. Zarifi, S. Farsinezhad, B.D. Wiltshire, M. Abdorrazaghi, N. Najia Mahdi, P. Kar, M. Daneshmand, K. Shankar, Effect of phosphonate monolayer adsorbate on the microwave photoresponse of TiO $_2$ nanotube membranes mounted on a planar double ring resonator, Nanotechnology 27 (2016), 375201, https://doi.org/10.1088/0957-4484/27/37/375201.
[26] D.M. Pozar, Microwave Engineering, J. Wiley, 2005. http://www.sidalc.net/cgi-bin/wxis.exe/?IsisScript=UCC.xis&method=post&formato=2&cantidad=1&expresion=mfn=059560. accessed June 15, 2018.
[27] J.-.K. Park, T.-.G. Kang, B.-.H. Kim, H.-.J. Lee, H.H. Choi, J.-.G. Yook, Real-time humidity sensor based on microwave resonator coupled with PEDOT: PSS conducting polymer film, Sci. Rep. 8 (2018) 439, https://doi.org/10.1038/s41598-017-18979-3.
[28] H.J. Liebe, G.A. Hufford, T. Manabe, A model for the complex permittivity of water at frequencies below 1 THz, Int. J. Infrared Millimeter Waves. 12 (1991) 659–675.
[29] S. Das, H. Sopha, M. Krbal, R. Zazpe, V. Podzemna, J. Prikryl, J.M. Macak, Electrochemical infilling of CuInSe2 within TiO2 nanotube layers and subsequent photoelectrochemical studies, ChemElectroChem. 4 (2017) 495–499, https://doi.org/10.1002/celc.201600763.
[30] A. Ebrahimi, J. Scott, K. Ghorbani, Microwave reflective biosensor for glucose level detection in aqueous solutions, Sens. Actuat. A Phys. 301 (2020), 111662, https://doi.org/10.1016/j.sna.2019.111662.
[31] M.H. Zarifi, B.D. Wiltshire, N. Mahdi, K. Shankar, M. Daneshmand, Distinguishing between deep trapping transients of electrons and holes in TiO2 nanotube arrays using planar microwave resonator sensor, ACS Appl. Mater. Interfaces. 10 (2018) 29857–29865, https://doi.org/10.1021/acsami.8b03629.
[32] A. Mohammadpour, P. Kar, B.D. Wiltshire, A.M. Askar, K. Shankar, Electron transport, trapping and recombination in anodic TiO<inf>2</inf>nano-tube arrays, Curr. Nanosci. 11 (2015), https://doi.org/10.2174/1573413711666150415230019.
[33] M.H. Zarifi, B. Wiltshire, N. Mahdi, P. Kar, K. Shankar, M. Daneshmand, Ultraviolet sensing using a TiO2 nanotube integrated high resolution planar microwave resonator device, Nanoscale 10 (2018) 4882–4889, https://doi.org/10.1039/C7NR06869G.
[34] H.K. Dunn, L.M. Peter, S.J. Bingham, E. Maluta, A.B. Walker, In situ detection of free and trapped electrons in dye-sensitized solar cells by photo-induced microwave reflectance measurements, J. Phys. Chem. C. 116 (2012) 22063–22072, https://doi.org/10.1021/jp3072074.
[35] X. Wang, Z. Feng, J. Shi, G. Jia, S. Shen, J. Zhou, C. Li, Trap states and carrier dynamics of TiO2 studied by photoluminescence spectroscopy under weak excitation condition, Phys. Chem. Chem. Phys. 12 (2010) 7083–7090, https://doi.org/10.1039/b925277k.
[36] J.M. Macak, A. Ghicov, R. Hahn, H. Tsuchiya, P. Schmuki, Photoelectrochemical properties of N-doped self-organized titania nanotube layers with different thickness, J. Mater. Res. 21 (2006) 2824–2828, https://doi.org/10.1557/jmr.2006.0344.
[37] R.P. Lynch, A. Ghicov, P. Schmuki, A photo-electrochemical investigation of self-organized TiO[sub 2] nanotubes, J. Electrochem. Soc. 157 (2010) G76, https://doi.org/10.1149/1.3276455.
[38] G. Cha, K. Lee, J.E. Yoo, M.S. Killian, P. Schmuki, Topographical study of TiO2 nanostructure surface for photocatalytic hydrogen production, Electrochim. Acta. 179 (2015) 423–430, https://doi.org/10.1016/j.electacta.2015.02.127.
[39] R. Zazpe, H. Sopha, J. Prikryl, M. Krbal, J. Mistrik, F. Dvorak, L. Hromadko, J. M. Macak, A 1D conical nanotubular TiO2/CdS heterostructure with superior photon-to-electron conversion, Nanoscale 10 (2018) 16601–16612, https://doi.org/10.1039/C8NR02418A.
[40] S. Nakade, Y. Saito, W. Kubo, T. Kitamura, and Y. Wada, S. Yanagida*, Influence of TiO2 nanoparticle size on electron diffusion and recombination in dye-sensitized TiO2 solar cells, (2003). doi:10.1021/JP034773W.
[41] Y.S. Kim, H.-.J. Jin, H.R. Jung, J. Kim, B.P. Nguyen, J. Kim, W. Jo, Reduced extrinsic recombination process in anatase and rutile TiO2 epitaxial thin films for efficient electron transport layers, Sci. Rep. 11 (2021) 6810, https://doi.org/10.1038/s41598-021-86422-9.
[42] S.O. Kasap, Principles of Electronic Materials and Devices, McGraw-Hill, New York, 2006.
[43] L.K. Fiddes, N. Yan, RFID tags for wireless electrochemical detection of volatile chemicals, Sens. Actuat., B Chem 186 (2013) 817–823, https://doi.org/10.1016/j.snb.2013.05.008.
[44] A. Bogner, C. Steiner, S. Walter, J. Kita, G. Hagen, R. Moos, Planar microstrip ring resonators for microwave-based gas sensing: design aspects and initial transducers for humidity and ammonia sensing, Sensors 17 (2017) 2422, https://doi.org/10.3390/s17102422.
[45] W.H. Hartwig, J.J. Hinds, Use of superconducting cavities to resolve carrier trapping effects in Cds, J. Appl. Phys. 40 (1969) 2020–2027, https://doi.org/10.1063/1.1657904.